Smooth Muscle Myosin 2 Filaments Dynamically Assemble and Stabilize During Induced Contractility

Margaret A. Bennett[1], Sasha G. Demeulenaere[1], Huini Wu[1], Hiral Patel[1], Stefano Sala[1], Elizabeth R. Longtine[1], Patrick W. Oakes[1], and Jordan R. Beach[1,✉]

[1]Department of Cell and Molecular Physiology, Stritch School of Medicine, Loyola University Chicago, Maywood, IL

Vascular smooth muscle cells (SMCs) line blood vessels throughout the body, where they dynamically alter vessel diameter to regulate blood pressure, provide structural integrity, and absorb shock on a beat-to-beat timescale. As smooth muscle function fails, profound vascular disease ensues, often with tragic results- even death. Smooth muscle myosin 2 (SM2) is the dominant motor protein that actuates contractility and allows SMCs to perform these vital functions. To function, SM2 monomers dynamically assemble into filaments, which upon SMC activation, associate with filamentous actin to drive contractility. Despite the critical contribution of SM2 to SMC function, foundational aspects of SM2 assembly and dynamics remain unexplored. To remedy this, we expressed EGFP-tagged SM2 in rat aortic smooth muscle cells (A7R5), which retained a cytosolic calcium and contractile response to the acetylcholine agonist carbachol. Using fluorescence recovery after photobleaching (FRAP), we observed rapid polymer exchange kinetics for SM2, more similar to non-muscle myosin 2 (NM2) than striated myosin 2s. Consistently, super-resolution imaging of SM2 and NM2 suggests they form filamentous co-polymers. Using a single cell filament assembly assay, we observed that the majority of SM2 is assembled in filaments at steady-state, but that SMC activation with carbachol rapidly increases SM2 assembly levels. Carbachol also reduced polymer exchange kinetics, suggesting stabilization of filaments during SMC activation. This carbachol-induced increase in SM2 assembly and decrease in exchange kinetics closely parallels the cytosolic calcium and contractility kinetics. Collectively, our data supports an updated model in which highly dynamic SM2 filaments assemble, are stabilized, and are activated to produce cell-scale contractile forces during SMC activation.

Smooth muscle | myosin 2 | assembly | Myh11

Correspondence: ***jbeach1@luc.edu***

Introduction

Smooth muscle is a fundamental component of the cardiovascular system. In major blood vessels, the smooth muscle layer (tunica media) comprises the vast majority of the vessel wall. This medial layer is dominated by vascular smooth muscle cells (SMCs) which are critical to the mechanical functions of blood vessels: to provide structural integrity, dynamically contract and relax to alter vessel diameter to modulate blood pressure, and absorb shock on a beat-to-beat timescale (1). SMC malfunction results in not only aberrant control of vascular tone and blood pressure, but in catastrophic failure of vascular integrity leading to thoracic aortic aneurysm and dissection (TAAD) (2, 3). Nearly 25% of TAAD can be attributed to a single gene mutation, with a plurality of those cases driven by mutations in the dominant contractile proteins smooth muscle myosin 2 (SM2) and smooth muscle actin (4). To understand how these mutations drive pathology, we must first understand how normal contractility operates in SMCs.

Contraction in SMCs is primarily powered by smooth muscle myosin 2 (SM2) acting on the actin cytoskeleton (5). SM2 is a member of the myosin 2 family, which also consists of striated myosin 2s (skeletal and cardiac) and non-muscle myosin 2s (NM2) (6). All myosin 2 "monomers" consist of two dimerizing heavy chains, two essential light chains, and two regulatory light chains. The extended coiled-coil of the heavy chain can reversibly associate with other monomers in parallel and antiparallel fashion to drive assembly of bipolar filaments (7, 8), placing motor domains at opposing ends. These filaments are the functional unit that interact with filamentous actin to drive contractile events.

Complicating this simple monomer:polymer equilibrium is a number of potential structural states (Fig. 1A). First, monomers can exist in a folded, inactive state, termed 10S, or an unfolded assembly-competent state, termed 6S (9–11). The folded 10S autoinhibited state has two key structural features: (1) the coiled-coil tail folds twice to wrap around the motor domains and stabilize the inhibited monomer; (2) the formation of the interacting heads motif (IHM), in which the motor domains dock on one another and fold back onto the N-terminus of the coiled-coil tail, thus preventing actin binding and ATP hydrolysis. The IHM and folded tail are not obligate, as the IHM has been observed and explored in filamentous striated muscle myosin 2s where it creates a partially-active (or partially-inactive) filament. Here, the IHM is the likely structural basis of the low energy super relaxed state (SRX) (12, 13), but this filamentous IHM/SRX state has not been clearly demonstrated for SM2 or NM2 in cells. Finally, to drive contraction, all myosin 2s can enter the open and active filamentous state. For SM2 and NM2, the conversion from the folded inactive 10S to the assembly competent 6S is largely dependent on phosphorylation of key residues on the regulatory light chain (RLC) (14, 15), which can be phosphorylated by calcium-mediated activation of myosin light chain kinase (MLCK) (16–18).

DRAFT

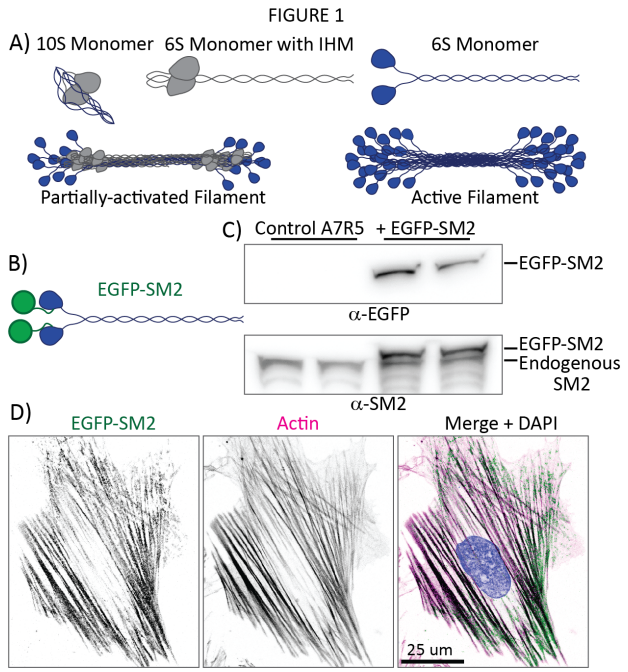

Fig. 1. Expression of SM2 in A7R5 SMCs. A) Cartoon of myosin 2 monomeric and filamentous structural states. B) Cartoon of 6S SM2 monomer tagged on the N-terminus with EGFP. C) Western blot of A7R5 cells untransfected (left lanes; duplicate) or transiently expressing EGFP-SM2 (right lanes; duplicate) probed with a-EGFP (top blot) or a-SM2 (bottom blot). D) Example images of A7R5 cell transiently expressing EGFP-SM2 (green), fixed and stained with phalloidin (actin; magenta).

Myosin 2 family members display disparate polymer exchange kinetics (the equilibrium between monomer and filament) and monomer:polymer ratios (total myosin 2 in monomer or filament at any given time). For example, non-muscle cells dynamically modulate non-muscle myosin 2 (NM2) filament assembly to control where and when they generate contractile force while maintaining about half of the total myosin 2 pool in filamentous form (19, 20). In contrast, striated myosin 2s assemble more stable filaments that generate contractile force independent of new filament assembly, with the vast majority of the total myosin 2 pool in filamentous form (21). Surprisingly, we do not know how smooth muscle cells modulate SM2 assembly and activation to generate contractile force, although there is a stated assumption that SMC contractility is driven by activation of pre-assembled SM2 filaments (22). Considering SM2 is genetically similar to non-muscle myosin 2 but perhaps more functionally similar to striated myosin 2s where it drives repeated uniaxial contractile events, how SM2 will behave in cells is difficult to predict without experimentation.

In this work we analyzed SM2 assembly and dynamics during induced contraction. We find that SM2 forms highly dynamic filaments during both steady-state and induced contraction. Furthermore, most SM2 is filamentous at steady-state and assembly increases upon induced contraction. This assembly kinetically parallels cytoplasmic calcium release and cell-scale force production. Therefore, our data supports a model in which SMC activation induces both nascent SM2 filament formation and activation of pre-existing filaments.

Results

A7R5 cells expressing EGFP-SM2 display calcium and contractile response to carbachol. A single SM2 gene (Myh11) with two splicing events produces four dominant isoforms (SM1A, SM1B, SM2A, SM2B; (23). The dominant isoform in vascular SMCs is SM1A (24, 25). Therefore, to better understand the dynamics of SM2 filaments in SMCs, we generated an expression plasmid with an EGFP coupled to the N-terminus of the SM1A heavy chain (hereafter EGFP-SM2; Fig. 1B). Western blot analysis of transient overexpression of EGFP-SM2 in A7R5 rat aortic SMCs demonstrated expression of the EGFP-SM2 shifted above endogenous SM2, as expected (Fig. 1C). High resolution imaging demonstrated that EGFP-SM2 associated with large actin stress fibers in the cells (Fig. 1D). Therefore, our EGFP-SM2 plasmid appears to be a faithful reporter of SM2 in these immortalized SMCs.

To confirm that our A7R5 cells are capable of induced contractility, we performed control experiments with the acetylcholine agonist carbachol. Carbachol treatment of GCaMP7s-expressing cells resulted in transient cytosolic calcium increases (Fig. 2A and 2C). In parallel, we performed traction force microscopy (TFM) to confirm that these cytosolic calcium increases were harnessed into contractile energy. We observed contractile force generation following carbachol treatment with a slight delay and extended duration

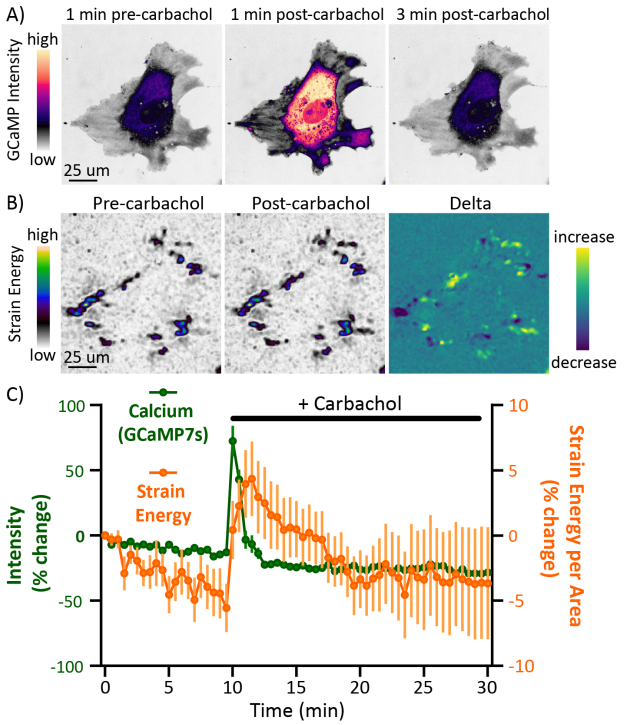

Fig. 2. A7R5 cells have a calcium and contractile response to carbachol. A and B) A7R5 cell expressing GCaMP7s was monitored for cytosolic calcium levels (A) while simultaneously being subject to traction force microscopy pre- and post-carbachol (B). GCaMP intensity and strain energy are displayed with iLUTs (scales on left). Pre-carbachol strain energy is the mean of 10 minutes pre-treatment and post-carbachol strain energy image is the mean of 10 minutes post-treatment. The delta between pre- and post-carbachol strain energy is displayed in the rightmost image. C) Quantitation of cytosolic calcium (green) and strain energy per area (orange) over time. Data plotted as mean +/- SEM for 15 cells from 3 experiments.

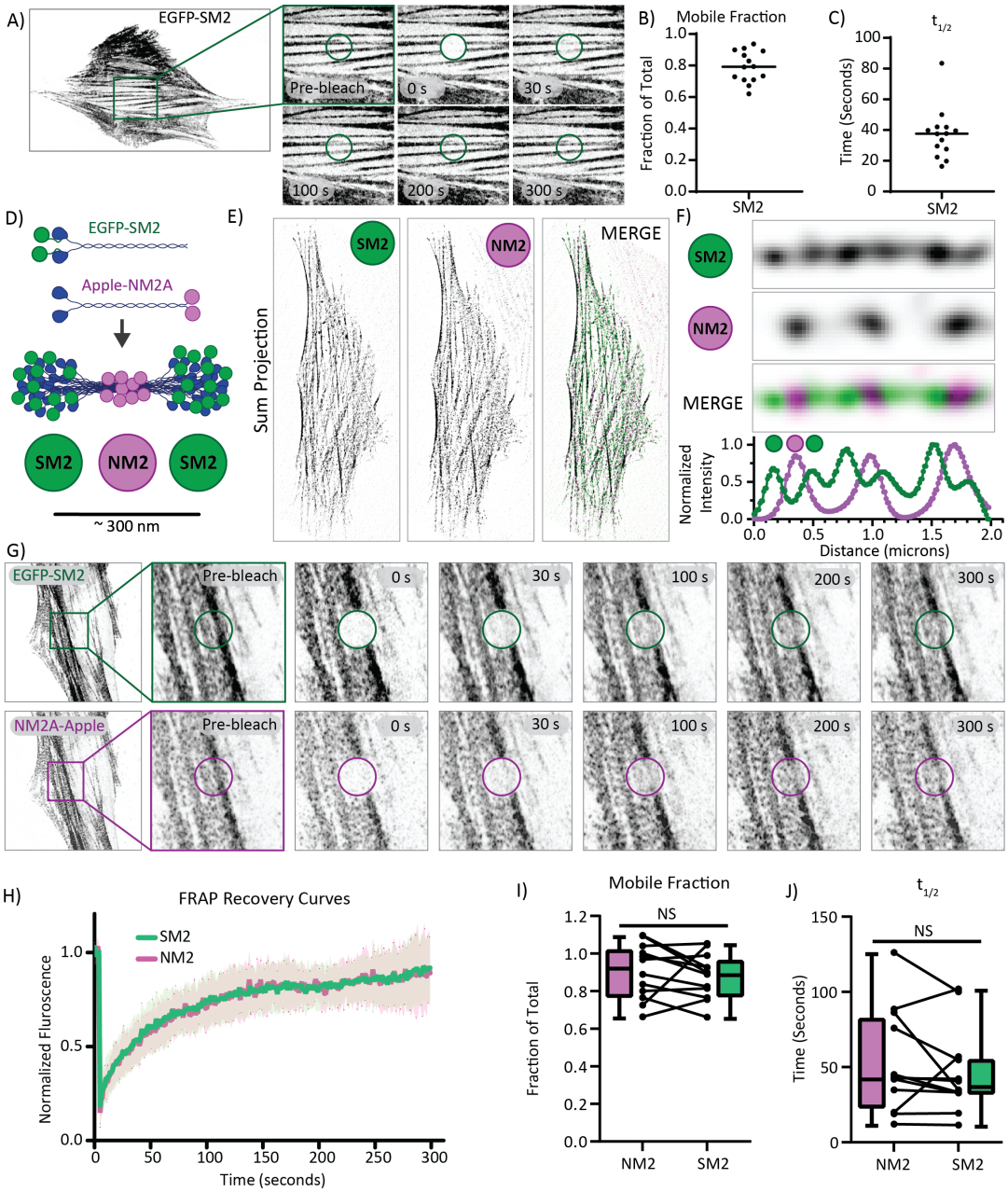

Fig. 3. SM2 Filaments are highly dynamic and similar to NM2. A) FRAP example A7R5 expressing EGFP-SM2. Bleach region indicated by green circle in insets. B and C) Mobile fraction (B) and t 1/2 (C) plotted for EGFP-SM2 from 13 cells from 3 independent experiments. D). Cartoon of co-assembled EGFP-SM2 and NM2A-mCherry. E) Co-transfection of EGFP-SM2 and NM2A-mApple in A7R5 cells were imaged with SIM and sum projected. Individual channels are displayed in inverted greyscale and merge is shown in the right panel. F) An individual actomyosin fiber was cropped from the cell in (E) and displayed at higher zoom for SM2, NM2 and merge. The lower plot is a line scan through the fiber normalized to maximum intensity for each channel. G) FRAP example of A7R5 expressing EGFP-SM2 (top row) and NM2A-mApple (bottom row). Bleach regions indicated by circles. H) Recovery curves of SM2 and NM2 plotted as mean +/- SEM for 12 cells from 3 independent experiments. I and J) Mobile fraction (I) and t1/2 (J) displayed as both box and whiskers (median +/- quartiles) and spaghetti plot. Dots in spaghetti plot represent individual cells for NM2 and SM2 with lines connecting cells. A paired t-tests was performed and there was no statistically significant difference between groups.

relative to the cytosolic calcium response (Fig. 2B and 2C), consistent with the calcium/MLCK-dependent signaling cascade that displays similar kinetics in intact smooth muscle tissue (26). Together these results indicate that while A7R5 cells are not primary SMCs, they retain a calcium-mediated contractile response to carbachol and can be used to investigate SM2 during induced activation.

SM2 filaments are dynamic with exchange kinetics similar to NM2. To investigate SM2 filament dynamics, fluorescence recovery after photobleaching (FRAP) was performed on A7R5 cells expressing EGFP-SM2. Here, we use the term "exchange" to refer to the movement of myosin 2 monomers into and out of filaments, and avoid the term "turnover", which might also refer to protein synthesis and degradation, which should not be relevant during our experimental timescales (minutes). Figure 3A shows an example FRAP experiment, with insets showing SM2 before bleaching and during recovery. FRAP quantification includes the mobile fraction, which is the fraction of filamentous SM2 ex-

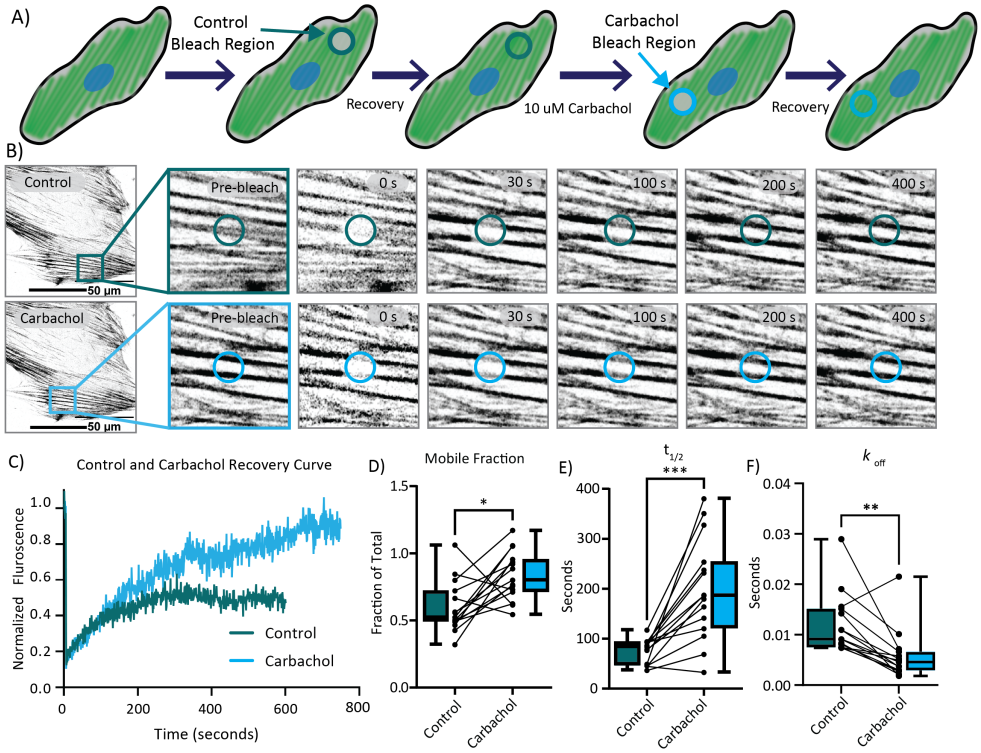

Fig. 4. SM2 filament dynamics are modulated upon induced contraction. A) Schematic of experimental design for FRAP of a single cell before and after addition of 10 uM carbachol. B) Fluorescence recovery of EGFP-SM2 in A7R5 pre- (green) and post (blue) carbachol. Circles indicate bleach region. C) Recovery curves of example cell in (B). D - F) Mobile fraction (D),t1/2 (E), and koff (F) of 15 cells from 3 independent experiments. Cells are represented as dots in a spaghetti plot where pre- and post-carbachol measurements for individual cells are connected. The same data is also displayed as box and whiskers (median +/- quartiles). Paired t-tests were formed between control and carbachol cells when measuring mobile fraction, t ½, and koff.

changing, and the t ½, which is the time it takes for half of the total exchange to occur. Our data reveal that SM2 filaments exchange readily (relatively high mobile fraction; Fig. 3B) and with rapid kinetics (relatively short t ½, Fig. 3C), relative to striated paralogs (27). This suggests SM2 forms highly dynamic filaments within SMCs that are more reminiscent of non-muscle myosin systems (19, 20) than striated muscle myosin systems (28).

The kinetic similarity and the genetic similarity between SM2 and NM2, along with the fact that SMCs express both myosin 2 paralogs, led us to more carefully investigate their relationship in our cell model. Previous studies have coupled different fluorophores on the head or tail of NM2 isoforms and imaged with structured illumination microscopy (SIM) to identify filaments and examine isoform co-assembly (29). This approach reveals alternating head-tail-head patterns about 300 nm in length, indicative of individual filaments or small filament stacks. We used a similar approach for SM2 and NM2 by co-expressing EGFP-SM2 and NM2A-mApple in A7R5 cells. SM2 and NM2A within the same filamentous structures would produce a green-magenta-green (head-tail-head) pattern (Fig. 3D). At the whole-cell scale, SM2 and NM2A were significantly co-localized along stress fibers (Fig. 3E). However, upon closer examination, we observed SM2 head domains about 300 nm apart flanking NM2A tails (Fig. 3E). While immuno-electron microscopy would more definitively confirm co-assembly in cells (30), our data suggest SM2 and NM2 isoforms can co-assemble in SMCs.

To better quantify the similarity in dynamics of SM2 and NM2, we performed simultaneous FRAP in the dual-expressing cells. The recovery curves for both proteins (Fig 3H) display nearly identical recovery. Quantification shows indistinguishable mobile fractions (Fig 3I) and t ½ (Fig 3J) indicating that both SM2 and NM2A filaments turnover rapidly and readily in SMCs. Collectively then, SM2 filaments in cultured SMCs co-localize with NM2 in filamentous structures that suggest co-assembly, and display rapid polymer exchange kinetics that are indistinguishable from NM2.

Differentiation to a "contractile" phenotype does not alter filament dynamics. SMCs can exist along a continuum between two phenotypes - contractile and synthetic. The contractile phenotype is found in healthy contracting blood vessels while the synthetic phenotype is more proliferative and migratory and is associated with pathological states (e.g. atherosclerosis) (31). We wanted to determine if SM2 assembly dynamics were altered upon induction of a prolonged contractile phenotype using serum starvation of A7R5 (32). Expression of contractile proteins in cells experiencing various serum conditions shows that serum starvation increases both SM2 and smooth muscle actin, confirming the protocol has pushed the cells towards a contractile phenotype (Fig S1A and S1B). However, FRAP analysis revealed that SM2 polymer exchange kinetics were unaltered, as there was no difference in mobile fraction or t½ between serum starved or non serum starved cells (Fig. S1C and S1D).

SM2 filament dynamics are modulated upon transiently-induced contraction. To examine the impact of transiently inducing contraction in SMCs to mimic physiological activation, we performed FRAP before and after the addition of carbachol, a cholinergic agonist which stimulates release of intracellular calcium via IP3 (33). To closely observe relative changes in polymer exchange kinetics, we

performed FRAP on a small region of an A7R5 expressing EGFP-SM2, then treated with carbachol, and immediately performed FRAP on a similar but distinct region of the same cell (Fig. 4A and 4B). This provided cell-specific internal controls to monitor relative changes in assembly dynamics. We observed an increase in mobile fraction (Fig. 4D), suggesting more complete filament exchange, but also an increase in t ½ (Fig. 4E), normally indicative of reduced exchange kinetics. However, because an increased mobile fraction with the same exchange kinetics would also lead to an increase in t ½, we analyzed the koff parameter in the exponential recovery equation, a more comparable exchange rate indicator. Indeed, we observed that koff was reduced upon treatment with carbachol (Fig. 4F), indicating reduced exchange kinetics and network stabilization.

Induced SMC contraction enhances SM2 filament assembly. To investigate SM2 assembly, we performed a single-cell imaging-based triton permeabilization assay to measure populations of monomeric and filamentous myosin. A7R5 cells expressing EGFP-SM2 were imaged to measure total EGFP-SM2 intensity, treated with or without carbachol, permeabilized with a triton buffer to remove monomeric SM2 pool, and re-imaged to measure remaining filamentous signal (Fig. 5A and 5B). Comparing intensity differences pre- and post-triton enables quantitative determination of monomer/filament ratios on a single cell basis. Control experiments with A7R5 cells expressing a diffuse EGFP reveal a complete loss of EGFP signal upon triton permeabilization, demonstrating cytosolic proteins are completely liberated in this assay (Fig. 5C). Control assembly levels for SM2 were 75% filamentous (Fig. 5D and Fig. S1E). We again observed no difference in this steady-state assembled fraction upon serum starvation (Fig. S1E). However, within one minute of carbachol addition assembly levels increased 10% and before decreasing towards steady-state levels in the ensuing minutes (Fig. 5D). Notably, these assembly kinetics parallel the cytosolic calcium response and traction force measurements during induced contractility (Fig. 2). Therefore, in addition to stabilization and activation of SM2 filaments, induced contraction results in nascent filament assembly.

Discussion

Our research leads to an updated model of SM2 filament assembly and contraction (Fig. 6). At steady-state, SM2 forms highly dynamic filaments with most, but not all of the SM2 in the filamentous state, likely co-assembled with NM2. We speculate that at steady-state, a portion of SM2 is in the filamentous IHM state. Upon SMC activation, elevated cytosolic calcium activates MLCK to phosphorylate RLC. This leads to unfolding of the 6S monomers into assembly competent 10S that assemble into new filaments, increasing overall filamentous SM2, decreasing monomeric populations, and decreasing exchange kinetics. In parallel, we speculate that MLCK phosphorylates RLC in filamentous IHM, enhancing activation of those existing filaments to drive physiological levels

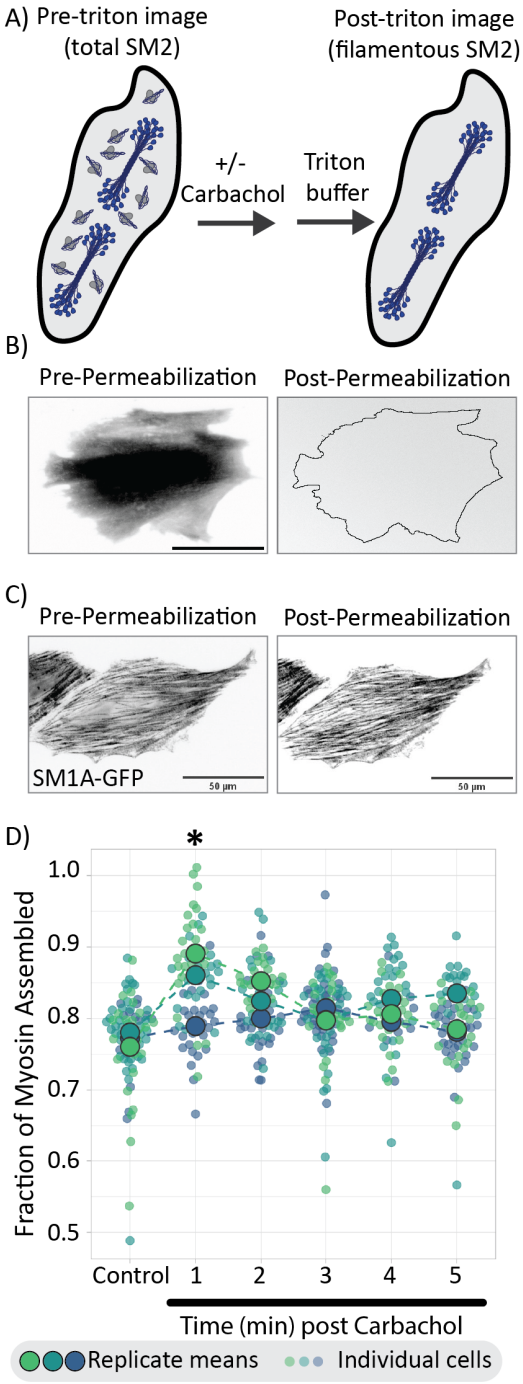

Fig. 5. Induced contraction of SMCs induces SM2 assembly. A) Cartoon illustrating single-cell assembly assay. Live A7R5 cells expressing EGFP-SM2 were imaged to determine total SM2 intensity (left). Cells were treated with or without 10 uM carbachol for the indicated time, monomeric SM2 was extracted using a triton buffer, and a second image was taken to determine the intensity of the remaining filamentous SM2. (B) Proof of concept A7R5 cells expressing EGFP were imaged pre- and post-permeabilization to demonstrate cytoplasmic proteins are fully extracted from the cell. C) Example image of EGFP-SM2 expressing A7R5 cell pre- and post-permeabilization. D) Quantification of the fraction of SM2 assembled in control cells and cells treated with 10 uM of carbachol for the indicated time. Small circles indicate individual cells. Larger dark circles indicate means of three independent experiments. A one-way Anova was used with multiple comparisons between each time point and control to statistically analyze the data.

of contraction. Our data is the first to investigate SM2 dynamics in cells. We observe rapid exchange kinetics between monomers and filaments. Considering the genetic similarity to NM2, this is not surprising. However, considering the function of SM2 is largely to drive uniaxial contractile events, similar to striated myosin 2s, the rationale for rapid exchange kinetics is not immediately apparent. In future studies, it will be important to determine exchange kinetics of endogenous SM2 in primary SMCs, ideally in intact tissue or organisms. This is obviously significantly more challenging than our current model system. Should similar exchange kinetics be observed in these future experiments, we speculate that rapid exchange kinetics enable rapid and tunable assembly levels that tune force production. Requisite changes in blood pressure or vascular tone could be rapidly achieved by modulating SM2 activation and assembly to a new setpoint.

Extracting more molecular level assembly information from our FRAP data during induced contraction is challenged by the timescales at play. During induced contraction, we observed a longer t ½ and shorter koff, indicative of reduced exchange kinetics. However, we also observed a larger mobile fraction, which indicates a greater fraction of total SM2 exchanging. In our other experiments, cytosolic calcium, SM2 assembly, and traction forces all peak within 1-2 minutes of carbachol-induced activation, afterwich they decay to steady-state levels within minutes. However, plateaus in our carbachol-treated FRAP data (required to fit exponential curves) require observation for 5-10 minutes. Therefore, the SM2 networks in our bleach regions are likely experiencing some exchange, as expected, but also significant filament assembly and subsequent disassembly, all within the experimental window. This complicates interpretation, but, overall, paints a picture of an SM2 filamentous network that is dynamic and responsive to SMC activation state. Future experiments using single molecule tracking of individual SM2 monomer lifetimes in filaments should enable the temporal resolution required to fully elucidate changes in exchange kinetics throughout an induced contraction event.

Smooth muscle is found in organs throughout the body, with each organ placing unique demands on the resident SMCs. For example, vascular smooth muscle performs tonic contraction to maintain vessel tone while gastrointestinal smooth muscle performs phasic contraction to move food through the GI tract. Splice variants of SM2 lead to unique SM2 isoform expression in different SMCs (34). Therefore, it would be interesting to determine if SM2 isoforms have unique exchange kinetics and assembly levels, and if these correlate with contractile properties of the SMCs in which they are expressed. Complicating this, of course, is the presence of NM2 isoforms and splice variants in each SMC population (23) that could also contribute to variation in contractile properties, especially if SM2 and NM2 are co-assembling. Further complexity could also arise from heterogenous myosin 2 subcellular functions within SMCs, as recent evidence demonstrated unique subcellular localization for SM2 and NM2 in freshly isolated primary cells (35). Finally, while the structure of NM2 bipolar filaments in cells

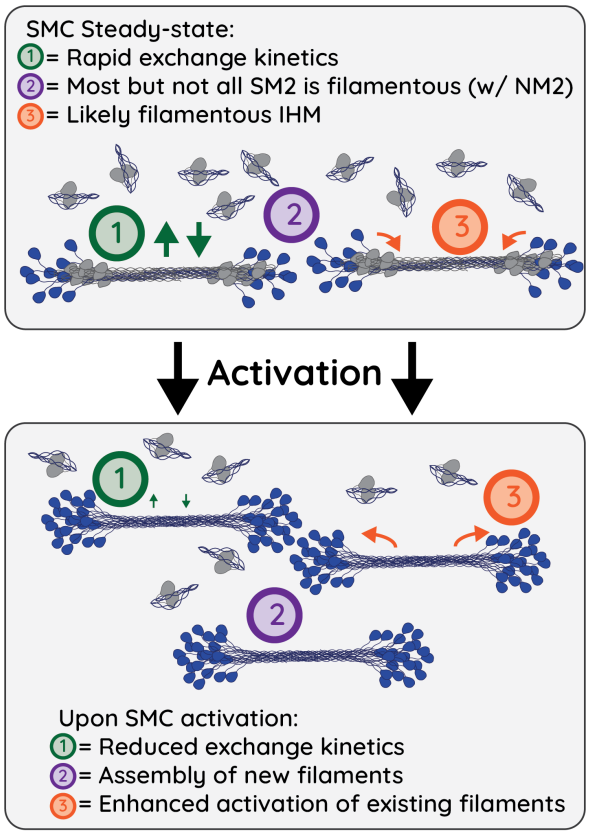

Fig. 6. Model of SM2 assembly at steady-state and upon activation. See Discussion for description.

is relatively well-established, the precise structural features of SM2 filaments in intact cells and tissues remains an active area of debate (36). Future studies to dissect unique and common biophysical properties of SM2 and NM2 filaments in SMCs should prove insightful.

Recent advances in cardiomyopathy-driving myosin mutations (primarily *MYH7*) suggest some mutations are either stabilizing or destabilizing the IHM to create hypo or hyper-contractile systems (37). Some pathologies driven by mutations in the NM2A heavy chain, collectively termed *MYH9*-Related Disease, are found along the coiled-coil tail and are thought to disrupt filament assembly and dynamics (38, 39). Many pathogenic or likely-pathogenic SM2 mutations have been reported (4), often resulting in aortic dysfunction, but most have not received any mechanistic scrutiny. We speculate that many of these SM2 mutations are altering IHM stability and/or altering filament assembly. As both hyper- and hypo-contractile SMCs could alter tissue compliance or tunability in an unfavorable manner, increasing or decreasing overall SM2 assembly and activity could drive pathology. Future studies to carefully dissect SM2 mutation impact on SM2 assembly dynamics should prove insightful.

Overall, our studies provide foundational details for SMC physiology and contraction, including highly dynamic filaments where both filament activation and filament assembly contribute to force production. Both dynamics and filament assembly are demonstrably modulated, and our studies open the door into elucidating precise and unexplored mech-

anisms (e.g. heavy chain phosphorylation) for both normal physiology and pathophysiology.

Materials and Methods

Mammalian Expression Plasmids. To make pEGFP-SM1A, a single gBlock was purchased from IDT that contained the 5' 420 basepairs of human SM1A, including the naturally occurring Sal1 restriction site, a short 5 basepair linker to facilitate restriction enzyme digestion, and the terminal 3' 616 base pairs, including the naturally occurring Blp1 restriction site and a terminal stop codon. This dsDNA was inserted into pEGFP-C1 after digestion with Bgl2 and Kpn1 restriction enzymes. The internal coding sequence of MYH11 not included in the gBlock was digested from full-length cDNA (MHS6278-202857900; Horizon Discovery) with Sal1 and Blp1 (4911 basepairs) and ligated into the pEGFP-C1-SM1A intermediate following digestion with Sal1 and Blp1. To make pLVX-GCaMP7s, jGCaMP7s was PCR amplified from pGP-CMV-jGCaMP7s (Addgene #104463). Following gel extraction, this dsDNA was inserted into the pLVX backbone with a CMV promoter using Gibson Assembly. GCaMP7s subject to PCR was sequence validated. Non-muscle myosin 2A-mApple was described previously (29).

Cell Culture and Transfection. Rat aortic smooth muscle cell line, A7R5 cells, were obtained from ATCC and cultured in DMEM (MT10013CV, Corning) supplemented with 10% fetal bovine serum (MT35-010-CV, Corning) and 1% antibiotic–antimycotic solution (MT30004CI, Corning). At 24 hours prior to each experiment, A7R5 cells were transfected with 2 ug total DNA using the lipid based transfection system LipoD 293 DNA transfection reagent (SignaGen, catalog SL100668). The A7R5 cells used for traction force microscopy were treated with lentivirus expressing GCaMP7s. A GCaMP7s positive population was obtained using fluorescence activated cell sorting. Lentiviral production was performed in HEK-293-FT cells using psPAX.2 and pMD2.G with LipoD 293 DNA transfection reagent. Lentiviral-containing media was collected at 48 and 72 hrs, filtered, and directly used for transformation of A7R5 cells. Plasmid psPAX2 was a gift from Didier Trono (Addgene plasmid #12260) and pMD2.G was a gift from Didier Trono (Addgene plasmid #12259). A7R5 cells were induced towards the contractile phenotype using serum starvation, whereby plated cells previously grown in full (10% serum) were given either 0% serum, 2.5% serum, or the control 10% serum for 24 hours (31)).

Single cell assembly assay. The single cell assembly assay was performed on A7R5 cells transiently overexpressing EGFP-SM2. Cells were plated in a 96 well coverglass bottom dish (655891, Greiner). Total EGFP-SM2 signal was collected for 16 positions per well. If applicable, small molecules were added and cells incubated for the indicated time. Then, triton buffer (5 uM PEG800, 100 mM PIPES, 150 mM NaCl, 1 mM EGTA, 1 mM MgCl2, .5% triton, 90% H20) was added to permeabilize the cells and release soluble EGFP-SM2. The exact same positions were re-imaged to collect the triton-insoluble EGFP-SM2 signal. Individual cells masked were manually identified using FIJI. Local background fluorescence and mean fluorescence intensity was measured for each cell before and after permeabilization. Fraction assembled was then calculated as background subtracted signal post-permeabilization relative to background subtracted signal pre-permeabilization.

FRAP. Fluorescence recovery after photobleaching (FRAP), was performed on A7R5 cells overexpressing EGFP-SM2 at 24 hrs post-transfection on a Zeiss LSM 880 Airyscan. Cells were imaged in Airyscan Fast mode at 1x Nyquist sampling for optimal confocal resolution at 1 Hz for up to 1200 seconds. A circular region (5 um diameter) was bleached using 405 nm, 458 nm, and 488 nm lasers at 100% laser power. For carbachol experiments, a cell was subject to FRAP, then carbachol was added, and then the same cell but unique bleach region was subject to FRAP again. Delay between carbachol addition and initiation of the second FRAP time-course was 30-60 seconds. FRAP analysis was performed in FIJI similar to previous protocols (40). Three ROIs were measured for each experiment - a bleach region, a control region within the cell, and a background region outside of the cell. Intensity was monitored over time in each region. Recovery within the bleach region was obtained after normalizing to the control region and subtracting the background region. Recovery curves were plotted in FIJI using the curve fitting plug in, fitting to a single exponential. The numbers given are used to calculate mobile fraction, t ½, and koff.

SIM imaging. A7R5 cells were transfected with EGFP-SM2 and mApple-NM2A. Images were collected on a Zeiss Elyra 7 Structured Illumination Microscope with a Plan-Apochromat 63x/1.4 NA oil DIC M27 objective. Scan Mode was FastFrame with 1.0 x zoom. Reconstruction was performed with SIM^2.

Western blot. Samples were scrape collected in 2x sample buffer or cells were pelleted and resuspended in 2x sample buffer. Samples were then boiled for 3-5 minutes, sonicated briefly, and used for analysis or stored at -20 C. Proteins were typically separated on 4-20% gels, unless separation of EGFP-SM2 and SM2 was required, in which case a 7.5% gel was used. Protein was transferred to a PVDF membrane using eBlot L1 (Genscript). Blocking was performed with 5% milk in PBST (PBS + 0.1% TritonX-100) and primary incubations were done overnight at 5 C. Primary antibodies were all used at 1:1,000 in blocking buffer (SM2, Abclonal #A4064; SMA Abclonal #A17910; EGFP, Santa Cruz #SC-9996)

Traction force microscopy. Traction force microscopy was performed as described previously (41, 42). Coverslips were prepared by incubating with a 2% solution of 3-aminopropyltrimethyoxysilane (313255000, Acros Organics) diluted in isopropanol, followed by fixation in 1%

glutaraldehyde (16360, Electron Microscopy Sciences) in ddH20. Polyacrylamide gels (shear modulus: 16 kPa—final concentrations of 12% acrylamide [1610140, Bio-Rad] and 0.15% bis-acrylamide [1610142, Bio-Rad]) were embedded with 0.04-µm fluorescent microspheres (F8789, Invitrogen) and polymerized on activated glass coverslips for 1 h at room temperature. After polymerization, gels were rehydrated overnight and coupled to human plasma fibronectin (FC010, Millipore) for 1 h at room temperature using the photoactivatable cross-linker Sulfo-Sanpah (22589, Pierce Scientific). Following fibronectin cross-linking, cells were plated on the gels and allowed to adhere overnight. The next day, images were taken of both the cells and underlying fluorescent beads. For kinetic analyses, images were collected every 30s for thirty minutes. The first ten minutes captured the steady-state, then 10 uM carbachol was added and the cells were imaged for another twenty minutes. Immediately after imaging, cells were removed from the gel using 0.05% SDS and a reference image of the fluorescent beads in the unstrained gel was taken.

Analysis of traction forces was performed using code written in Python according to previously described approaches (42, 43). Prior to processing, images were flat-field corrected and the reference bead image was aligned to the bead image with the cell attached. Displacements in the beads were calculated using an optical flow algorithm in OpenCV (Open Source Computer Vision Library, https://github/itseez/opencv) with a window size of 8 pixels. Traction stresses were calculated using the FTTC approach (42, 44) as previously described, with a regularization parameter of 6.1 × 10–4. The strain energy was calculated by summing one-half the product of the strain and traction vectors in the region under the cell (41) and normalized by the cell area as measured using the GCaMP7s image of the cell.

Stats. Statistics were performed using the GraphPad Prism. Asterisks are used to convey statistical significance are as follows: * for $p < 0.05$, ** for $p < 0.005$, *** for $p < 0.0005$.

Acknowledgements

Research reported in this publication was supported by the Maximizing Investigators' Research Award (MIRA) (R35) from the National Institute of General Medical Sciences (NIGMS) of the National Institutes of Health (NIH) under grant number R35GM138183 to JRB.

Bibliography

1. Yingzhi Zhuge, Jian Zhang, Fanyu Qian, Zhengwang Wen, Chao Niu, Ke Xu, Hao Ji, Xing Rong, Maoping Chu, and Chang Jia. Role of smooth muscle cells in cardiovascular disease. *Int. J. Biol. Sci.*, 16(14):2741–2751, August 2020.
2. Utako Yokoyama, Noriaki Arakawa, Ryo Ishiwata, Shota Yasuda, Tomoyuki Minami, Motohiko Goda, Keiji Uchida, Shinichi Suzuki, Masataka Matsumoto, Nobusato Koizumi, Masataka Taguri, Hisashi Hirano, Koichi Yoshimura, Hitoshi Ogino, Munetaka Masuda, and Yoshihiro Ishikawa. Proteomic analysis of aortic smooth muscle cell secretions reveals an association of myosin heavy chain 11 with abdominal aortic aneurysm. *Am. J. Physiol. Heart Circ. Physiol.*, 315(4):H1012–H1018, October 2018.
3. Hariyadarshi Pannu, Van Tran-Fadulu, Christina L Papke, Steve Scherer, Yaozhong Liu, Caroline Presley, Dongchuan Guo, Anthony L Estrera, Hazim J Safi, Allan R Brasier, G Wesley Vick, A J Marian, C S Raman, L Maximilian Buja, and Dianna M Milewicz. MYH11 mutations result in a distinct vascular pathology driven by insulin-like growth factor 1 and angiotensin II. *Hum. Mol. Genet.*, 16(20):2453–2462, October 2007.
4. Norifumi Takeda and Issei Komuro. Genetic basis of hereditary thoracic aortic aneurysms and dissections. *J. Cardiol.*, 74(2):136–143, August 2019.
5. B J Panner and C R Honig. Filament ultrastructure and organization in vertebrate smooth muscle. contraction hypothesis based on localization of actin and myosin. *J. Cell Biol.*, 35 (2):303–321, November 1967.
6. M Amanda Hartman and James A Spudich. The myosin superfamily at a glance. *J. Cell Sci.*, 125(Pt 7):1627–1632, April 2012.
7. J M Squire. General model for the structure of all myosin-containing filaments. *Nature*, 233 (5320):457–462, October 1971.
8. John M Squire. Muscle myosin filaments: cores, crowns and couplings. *Biophys. Rev.*, 1 (3):149, September 2009.
9. Deanna L Milton, Amy N Schneck, Dominique A Ziech, Mariam Ba, Kevin C Facemyer, Andrew J Halayko, Jonathan E Baker, William T Gerthoffer, and Christine R Cremo. Direct evidence for functional smooth muscle myosin II in the 10S self-inhibited monomeric conformation in airway smooth muscle cells. *Proc. Natl. Acad. Sci. U. S. A.*, 108(4):1421–1426, January 2011.
10. H Suzuki, H Onishi, K Takahashi, and S Watanabe. Structure and function of chicken gizzard myosin. *J. Biochem.*, 84(6):1529–1542, 1978.
11. K M Trybus, T W Huiatt, and S Lowey. A bent monomeric conformation of myosin from smooth muscle. *Proc. Natl. Acad. Sci. U. S. A.*, 79(20):6151–6155, 1982.
12. Pleuni Hooijman, Melanie A Stewart, and Roger Cooke. A new state of cardiac myosin with very slow ATP turnover: a potential cardioprotective mechanism in the heart. *Biophys. J.*, 100(8):1969–1976, April 2011.
13. Lorenzo Alamo, Dan Qi, Willy Wriggers, Antonio Pinto, Jingui Zhu, Aivett Bilbao, Richard E Gillilan, Songnian Hu, and Raúl Padrón. Conserved intramolecular interactions maintain myosin Interacting-Heads motifs explaining tarantula muscle Super-Relaxed state structural basis. *J. Mol. Biol.*, 428(6):1142–1164, March 2016.
14. R S Adelstein and M A Conti. Phosphorylation of platelet myosin increases actin-activated myosin ATPase activity. *Nature*, 256(5518):597–598, 1975.
15. R Craig, R Smith, and J Kendrick-Jones. Light-chain phosphorylation controls the conformation of vertebrate non-muscle and smooth muscle myosin molecules. *Nature*, 302(5907): 436–439, 1983.
16. M Ikebe, D J Hartshorne, and M Elzinga. Identification, phosphorylation, and dephosphorylation of a second site for myosin light chain kinase on the 20,000-dalton light chain of smooth muscle myosin. *J. Biol. Chem.*, 261(1):36–39, January 1986.
17. J R Sellers, M D Pato, and R S Adelstein. Reversible phosphorylation of smooth muscle myosin, heavy meromyosin, and platelet myosin. *J. Biol. Chem.*, 256(24):13137–13142, December 1981.
18. M A Corson, J R Sellers, R S Adelstein, and M Schoenberg. Substance P contracts bovine tracheal smooth muscle via activation of myosin light chain kinase. *Am. J. Physiol.*, 259(2 Pt 1):C258–65, August 1990.
19. Mark T Breckenridge, Natalya G Dulyaninova, and Thomas T Egelhoff. Multiple regulatory steps control mammalian nonmuscle myosin II assembly in live cells. *Mol. Biol. Cell*, 20(1): 338–347, January 2009.
20. Miguel Vicente-Manzanares, Jessica Zareno, Leanna Whitmore, Colin K Choi, and Alan F Horwitz. Regulation of protrusion, adhesion dynamics, and polarity by myosins IIA and IIB in migrating cells. *J. Cell Biol.*, 176(5):573–580, February 2007.
21. Neil B Wood, Colleen M Kelly, Thomas S O'Leary, Jody L Martin, and Michael J Previs. Cardiac myosin filaments are maintained by stochastic protein replacement. *Mol. Cell. Proteomics*, page 100274, July 2022.
22. R Clinton Webb. Smooth muscle contraction and relaxation. *Adv. Physiol. Educ.*, 27(1-4): 201–206, December 2003.
23. Thomas J Eddinger and Daniel P Meer. Myosin II isoforms in smooth muscle: heterogeneity and function. *Am. J. Physiol. Cell Physiol.*, 293(2):C493–508, August 2007.
24. S L White, M Y Zhou, R B Low, and M Periasamy. Myosin heavy chain isoform expression in rat smooth muscle development. *Am. J. Physiol.*, 275(2):C581–9, August 1998.
25. M E DiSanto, R H Cox, Z Wang, and S Chacko. NH2-terminal-inserted myosin II heavy chain is expressed in smooth muscle of small muscular arteries. *Am. J. Physiol. Cell Physiol.*, 272 (5):C1532–C1542, May 1997.
26. E Isotani, G Zhi, K S Lau, J Huang, Y Mizuno, A Persechini, R Geguchadze, K E Kamm, and J T Stull. Real-time evaluation of myosin light chain kinase activation in smooth muscle tissues from a transgenic calmodulin-biosensor mouse. *Proc. Natl. Acad. Sci. U. S. A.*, 101 (16):6279–6284, 2004.
27. Koichi Ojima, Emi Ichimura, Yuya Yasukawa, Jun-Ichi Wakamatsu, and Takanori Nishimura. Dynamics of myosin replacement in skeletal muscle cells. *Am. J. Physiol. Cell Physiol.*, 309 (10):C669–79, November 2015.
28. Dale D Tang. The dynamic actin cytoskeleton in smooth muscle. *Adv. Pharmacol.*, 81:1–38, 2018.
29. Jordan R Beach, Lin Shao, Kirsten Remmert, Dong Li, Eric Betzig, and John A Hammer, 3rd. Nonmuscle myosin II isoforms coassemble in living cells. *Curr. Biol.*, 24(10):1160–1166, May 2014.
30. M S Shutova, W A Spessott, C G Giraudo, and T Svitkina. Endogenous species of mammalian nonmuscle myosin IIA and IIB include activated monomers and heteropolymers. *Curr. Biol.*, 24(17):1958–1968, 2014.
31. Joseph M Miano, Edward A Fisher, and Mark W Majesky. Fate and state of vascular smooth muscle cells in atherosclerosis. *Circulation*, 143(21):2110–2116, May 2021.
32. B W Kimes and B L Brandt. Characterization of two putative smooth muscle cell lines from rat thoracic aorta. *Exp. Cell Res.*, 98(2):349–366, March 1976.
33. Hiroyasu Satoh. Modulation of ca2+-activated k+ current by isoprenaline, carbachol, and phorbol ester in cultured (and fresh) rat aortic vascular smooth muscle cells. *General Pharmacology: The Vascular System*, 27(2):319–324, March 1996.
34. Y Hamada, M Yanagisawa, Y Katsuragawa, J R Coleman, S Nagata, G Matsuda, and T Masaki. Distinct vascular and intestinal smooth muscle myosin heavy chain mRNAs are encoded by a single-copy gene in the chicken. *Biochem. Biophys. Res. Commun.*, 170(1): 53–58, July 1990.
35. Kuldeep Singh, Anne B Kim, and Kathleen G Morgan. Non-muscle myosin II regulates aortic

stiffness through effects on specific focal adhesion proteins and the non-muscle cortical cytoskeleton. *J. Cell. Mol. Med.*, February 2021.
36. Isabel J Sobieszek and Apolinary Sobieszek. Myosin assembly of smooth muscle: from ribbons and side polarity to a row polar helical model. *J. Muscle Res. Cell Motil.*, July 2022.
37. Lorenzo Alamo, James S Ware, Antonio Pinto, Richard E Gillilan, Jonathan G Seidman, Christine E Seidman, and Raúl Padrón. Effects of myosin variants on interacting-heads motif explain distinct hypertrophic and dilated cardiomyopathy phenotypes. *Elife*, 6, June 2017.
38. M J Kelley, W Jawien, T L Ortel, and J F Korczak. Mutation of MYH9, encoding non-muscle myosin heavy chain a, in May-Hegglin anomaly. *Nat. Genet.*, 26(1):106–108, September 2000.
39. Kasturi Pal, Roberta Nowak, Neil Billington, Rong Liu, Arit Ghosh, James R Sellers, and Velia M Fowler. Megakaryocyte migration defects due to nonmuscle myosin IIA mutations underly thrombocytopenia in MYH9-Related disease. *Blood*, February 2020.
40. David J Rademacher, Maleen Cabe, and Joanna C Bakowska. Fluorescence recovery after photobleaching of yellow fluorescent protein tagged p62 in aggresome-like induced structures. *J. Vis. Exp.*, (145), March 2019.
41. Patrick W Oakes, Shiladitya Banerjee, M Cristina Marchetti, and Margaret L Gardel. Geometry regulates traction stresses in adherent cells. *Biophys. J.*, 107(4):825–833, August 2014.
42. Benedikt Sabass, Margaret L Gardel, Clare M Waterman, and Ulrich S Schwarz. High resolution traction force microscopy based on experimental and computational advances. *Biophys. J.*, 94(1):207–220, January 2008.
43. Jana Hanke, Dimitri Probst, Assaf Zemel, Ulrich S Schwarz, and Sarah Köster. Dynamics of force generation by spreading platelets. *Soft Matter*, 14(31):6571–6581, August 2018.
44. James P Butler, Iva Marija Tolić-Nørrelykke, Ben Fabry, and Jeffrey J Fredberg. Traction fields, moments, and strain energy that cells exert on their surroundings. *Am. J. Physiol. Cell Physiol.*, 282(3):C595–605, March 2002.

Supplementary Information

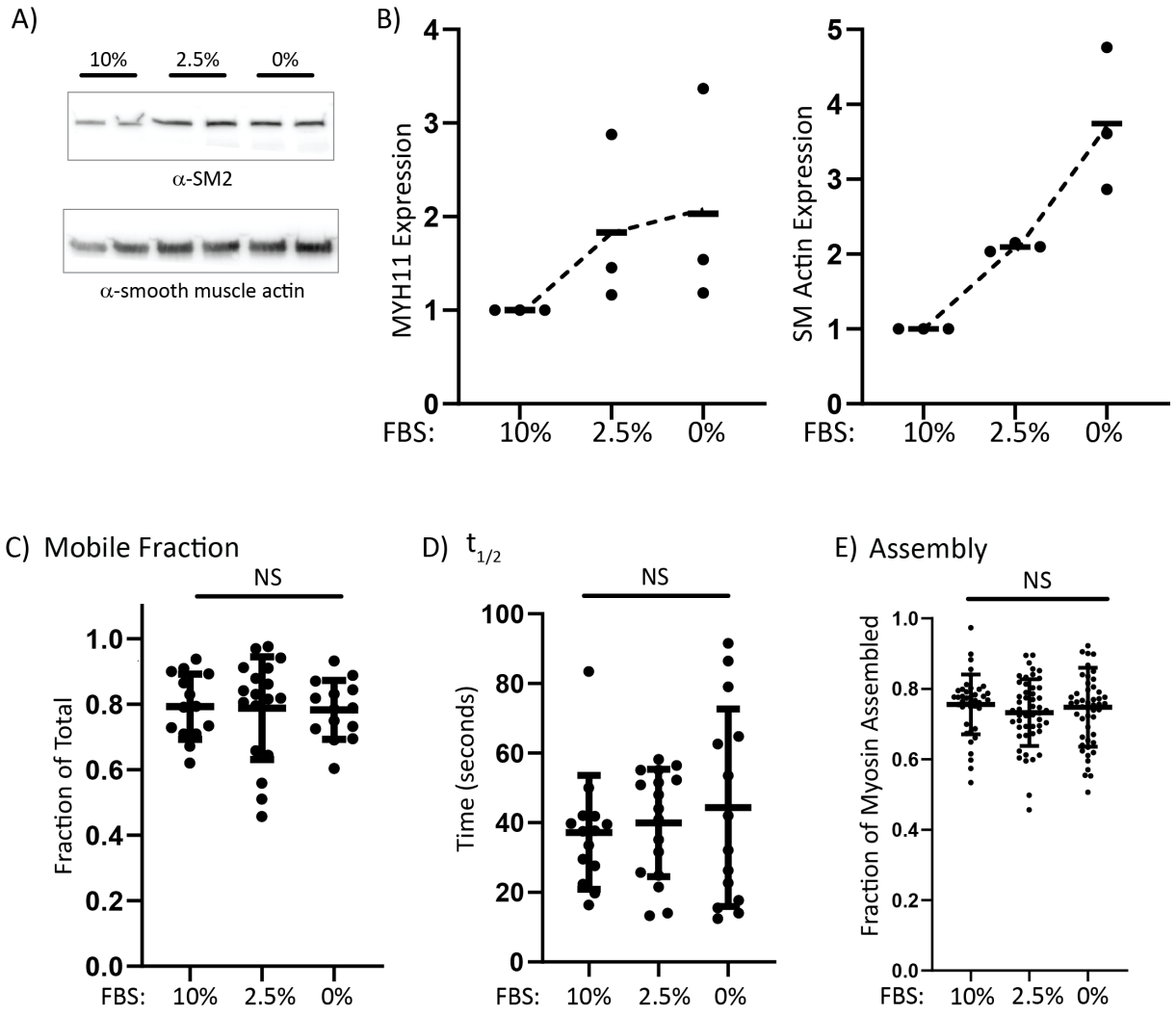

Fig. S1. Differentiation to a more contractile phenotype does not change filament assembly or dynamics. A and B) A7R5 cells cultured in media with 10%, 2.5%, or 0% FBS in duplicate were subject to western blot analysis with a-SM2 (top blot) and a-smooth muscle actin (bottom blot). Cumulative data plotted in B as mean +/- SD from 6 samples per condition from 3 independent experiments.C and D) FRAP was performed on A7R5 cells expressing EGFP-SM2 cultured in media containing the indicated levels of FBS. Mobile fraction and t ½ plotted as the mean of 14-18 cells per condition over 3 individual experiments. E) Single cell assembly assay was performed on A7R5 cells expressing EGFP-SM2 cultured in media containing the indicated levels of FBS. Data plotted from 3 independent experiments. One way ANOVA performed between groups and showed no difference.